



Characterization of the solvent specific evaporation from a carbon nanotube buckypaper doped by goethite nanowires

Ildikó Y. Tóth^{*}, Gábor Veress, Imre Szenti, Ákos Kukovecz

University of Szeged, Interdisciplinary Excellence Centre, Department of Applied and Environmental Chemistry, H-6720, Rerrich Béla tér 1, Szeged, Hungary

ARTICLE INFO

Keywords:

Carbon nanotube
Goethite nanowire
Buckypaper
Wetting
Evaporation profile
Thermography

ABSTRACT

Non-functionalized carbon nanotube based self-supporting buckypaper doped by goethite nanowire was prepared (characterized by TEM, XRD, FTIR, DLS, electrophoresis, SEM) and studied to determine the wetting and evaporation properties of the composite. The wetting and vaporization of water, methanol, ethanol, 2-propanol, acetone, 1,4-dioxane were monitored at 50 °C parallel by weight and electrical resistance measurements and also by thermography in case of water and ethanol. Based on the weight measurements, the different stages of the evaporation (evaporation of sessile droplet, vaporization of the condensed and adsorbed solvents from the porous system) could be distinguished, which could be characterized by their evaporation rate and the amount of liquid remaining in the porous system at the end of the given stages. The evaporation profiles determined from the electrical resistance measurements are characteristic for the evaporating solvents, similar to the mass measurement results. The details of the wetting process can be analyzed by thermography based on the area and temperature of the wetted region. The relationship between the physical properties of the solvents and the parameters characteristic for the evaporation obtained from the weight and electrical resistance measurements was statistically analyzed using Pearson correlation coefficients method. There is a very high correlation for example between surface tension and t_f (PCC = 0.971) or t_g (PCC = 0.992), and also between the boiling point and $Area_{(R)}$ (PCC = 0.929). These results allow us to predict the possibility of this setup in a potential future analytical application.

1. Introduction

Nanotechnology deals with materials in the size range of 1–100 nm (in the new literature sometimes this definition is extended up to 150 nm), which nanoparticles have unique properties compared to bulk materials. They are widely studied in research and development in various fields such as environmental, medical, biomedical, industrial, electrical, *etc.* [1–4]. These developments have highlighted the importance of the classical topics of wetting, droplet spreading and evaporation, which phenomena govern several key technological applications like micro-fluidics [3,5,6], oil recovery [4,7], controlled deposition of self-assembled surface coatings [8,9] or inject printing [10], just to name a few.

Carbon nanotubes (CNTs) are one of the widely used raw materials in nanotechnology (e.g., electronics, optics, composite materials and biomedical science) due to their special properties (extraordinary electrical conductivity, high thermal conductivity, low density, high tensile strength, *etc.*) [11–18]. The self-supporting paper-like film of carbon

nanotubes (buckypaper, BP) has long been used as a handleable macroscopic form of multiwall CNTs. Buckypaper is a self-supporting, mesoporous, permeable, electrically conducting mat, which have several interesting applications like radio frequency filters [19], artificial muscles [20], mechanical sensors [21], cigarette smoke filter [22], semiconducting layers in different types of electronic, optoelectronic, and sensor systems [23].

The iron oxides/hydroxides/oxo-hydroxides had been widely studied for several reasons [24]: their minerals are abundant in nature, they can be easily synthesized in the laboratory, they are relatively inexpensive, they are good adsorbents for organic and inorganic materials [25], they are good catalysts [26], and they are suitable for many different medical and bioengineering applications [27], as well. One of the main forms of these minerals is the goethite (α -FeOOH), which is a widespread soil mineral and has been well known since ancient times for its use as a pigment [24]. The synthetic goethite particles are widely used in catalytic reactions [28–30] and as an efficient adsorbent nanomaterial in water treatment [25], for example removal of organic

^{*} Corresponding author.

E-mail address: ildiko.toth@chem.u-szeged.hu (I.Y. Tóth).

<https://doi.org/10.1016/j.molliq.2023.122816>

Received 13 May 2023; Received in revised form 8 August 2023; Accepted 10 August 2023

Available online 14 August 2023

0167-7322/© 2023 Elsevier B.V. All rights reserved.

compounds [31], nitrobenzene [28], methylene blue [32], ammonia [30], Co(II) and Ni(II) [33], Cr(IV) [29] or arsenic [34,35].

The evaporation of a liquid sessile droplet is a multifaceted topic despite its apparent simplicity and ubiquity. The vaporization of sessile droplets plays a key role in a wide range of industrial and biomedical applications, including desalination, inkjet printing, painting, cooling technologies, evaporative lithography, thin film coating, surface patterning, agrochemical spraying of plants, biological and chemical assays, DNA synthesis, protein crystallography, etc. [36–40].

The evaporation of sessile droplets on non-porous solid surfaces can be categorized into three basic scenarios: *i*) evaporation of simple fluids on plain surfaces, *ii*) vaporization of simple solutions on micro and/or nano-structured surfaces, *iii*) evaporation of fluids containing dispersed nanoparticles from plain surfaces [41–43]. However, multiple complex phenomena take place simultaneously when a liquid droplet contacts the surface of a porous material, combining several consecutive and parallel steps, like: drop impact on the surface, spreading and wetting, solvent diffusion into pores, capillary filling, adsorption, evaporation from the surface and pores, etc. [44–47].

The evaporation of a sessile droplet can be studied by several experimental methods: transmission electron microscopy [48], environmental scanning electron microscopy [49], high speed camera recordings [50,51], thermal imaging [52], etc. The evaporation of sessile droplets can also be followed by an equipment, which can guide simultaneous weight monitoring, electric resistance measurement and infrared imaging at a controlled temperature (typically at 50 °C). There are several experimental results characteristic for the evaporation process, the most important ones being the total evaporation time, time of evaporation only from the surface, full width at half maximum of the time-dependent weight and resistance curves, evaporation rate, initial area of the droplet, and the wetted area at the moment of total evaporation from the surface, etc. [41,44,52].

Many composites containing goethite and carbon nanotube can be found in the literature, for example composites prepared for high-performance supercapacitors [53], for bifunctional catalyst in rechargeable zinc-air batteries [54] or for arsenic removal [55,56]. However, to our best knowledge, the wetting and evaporation properties of this type of composites have not yet been characterized comprehensively, although knowing these is important for understanding, planning, and tuning the aforementioned applications.

The main goal of the present work was to prepare porous buckypaper from non-functionalized carbon nanotube (η CNT) doped by goethite nanowire (GNW), and to obtain a more detailed picture of the wetting and evaporation properties of the GNW/ η CNT BP sample. The evaporation of different solvents (water, methanol, ethanol, 2-propanol, acetone and 1,4-dioxane) from the surface of the GNW/ η CNT BP sample was characterized by simultaneous weight monitoring, high speed imaging and thermography. This knowledge even can contribute to the development of a novel, evaporation based analytical method [41,44] by the statistical analysis of the experimentally determined evaporation parameters.

2. Materials and methods

2.1. Materials

The carbon nanotubes were synthesized in a quartz reactor by 2 h of catalytic chemical vapour deposition from a $\text{C}_2\text{H}_4:\text{N}_2$ (30:300 cm^3/min) gas mixture at 650 °C over $\text{Fe,Co}/\text{Al}_2\text{O}_3$ (2.5, 2.5 wt% metal loading) catalyst. The synthesized nanotubes were purified by repeating 4 h of refluxing in 10 mol/dm^3 aqueous NaOH, then 4 h in cc. HCl solution (37 wt%) four times. The prepared CNTs were washed by milliQ water and dried at 80 °C for a day [57]. No other functionalization process was used during the synthesis, so the nanomaterial produced in this way can be considered a non-functionalized carbon nanotube (η CNT).

The goethite nanomaterials were prepared by oxidation-

precipitation method from the water -based solution of FeSO_4 (20 mL milliQ water, 13.6 g $\text{FeSO}_4 \cdot 7\text{H}_2\text{O}$), using NaOH solution for precipitation (45 mL milliQ water, 4.4 g NaOH) and NaNO_3 for oxidation (35 mL milliQ water, 12.3 g NaNO_3). The FeSO_4 and NaNO_3 solutions were added dropwise to the NaOH solution, during continuous magnetic stirring. The synthesis was performed at room temperature and under normal atmosphere. The yellow product was purified by centrifugation and dried at 80 °C for a day. The synthesized material is assumed to be goethite nanowire (GNW).

Self-supporting goethite containing carbon nanotube film (buckypaper, BP) was prepared from 6.3 mg of η CNTs and 0.7 mg of GNW, suspended separately in 50 cm^3 and 20 cm^3 of N,N-dimethylformamide (DMF) solvent, by 30 min of sonication in an Elmasonic S 80H ultrasonic bath. The two suspensions were mixed and their mixture was sonicated for an additional 30 min. The suspension was filtered through 0.45 μm Whatman nylon filters ($d = 25$ mm) using dead-end filtration with an effective pressure difference of 960 mbar. The sample was dried overnight, on the filters in 80 °C air and peeled off afterwards. The prepared buckypapers contain 90 wt% non-functionalized carbon nanotube and 10 wt% goethite nanowire (GNW/ η CNT BP).

2.2. Methods

2.2.1. Characterization of the nanoparticles and buckypaper

The size of the nanoparticles was characterized by a FEI-Tecnai G2/20/X-TWIN transmission electron microscope (TEM), with the accelerating voltage of 200 kV applied. One drop of highly diluted suspension was dried on holey carbon-coated copper grids of 300 mesh. The average size distribution was determined by evaluating more than 200 particles using the ImageJ software.

The quality of the nanomaterials was verified by powder X-ray diffraction (XRD) technique. The XRD patterns were obtained with a Rigaku Miniflex-II instrument operating with $\text{Cu-K}\alpha$ radiation ($\lambda = 1.5406$ Å). The 2θ Bragg angles were scanned over a range of 20–60° at a rate of 1.0° min^{-1} . The GNW was measured from its suspension dried on a sample holder in a thin layer.

Attenuated total reflectance-Fourier transform infrared spectroscopy (ATR-FTIR) was used to verify the quality and determine the surface functional groups of the prepared nanomaterials. FTIR-ATR spectra were recorded with a Bruker Vertex 70 FTIR spectrometer coupled to a Bruker Hyperion 2000 IR microscope. The absorbance of the samples was measured in reflection mode over the 600–4000 cm^{-1} range (with resolution of 4 cm^{-1}), accumulating 140 scans. The suspensions of η CNT and GNW were dropped and dried onto the aluminium sample holder. The background spectra were measured on clean and dry germanium crystal.

For characterization of the particle size and the aggregation state of nanoparticles in water-based systems, the average hydrodynamic diameter (Z-Ave) of η CNT and GNW particles were determined at 25 ± 0.1 °C using the dynamic light scattering (DLS) method, an apparatus Nano ZS (Malvern) with a 4 mW He-Ne laser source ($\lambda = 633$ nm) operating in backscattering mode at an angle of 173°. The dispersions contained 70 mg/dm^3 of the nanoparticles. Prior to the measurements, the samples were homogenized in an ultrasonic bath for 10 s, after which 2 min relaxation was allowed. Any changes in the aggregation state of the nanoparticles in aqueous dispersions was characterized by the hydrodynamic diameter (Z-Ave). The effect of pH variation (between 2 and 11) was studied at 10 mmol/dm^3 NaCl. For evaluation, we used the second- or third-order cumulant fit of the autocorrelation functions, depending on the degree of polydispersity.

Electrophoretic mobilities of the nanoparticles dispersions were measured at 25 ± 0.1 °C in the same Nano ZS (Malvern) apparatus using disposable zeta cells (DTS 1061). The pH-range and the ionic strength were identical to those in the DLS experiments. The Smoluchowski equation was applied to convert electrophoretic mobilities to electrokinetic potential values. The accuracy of the measurements was ± 5 mV.

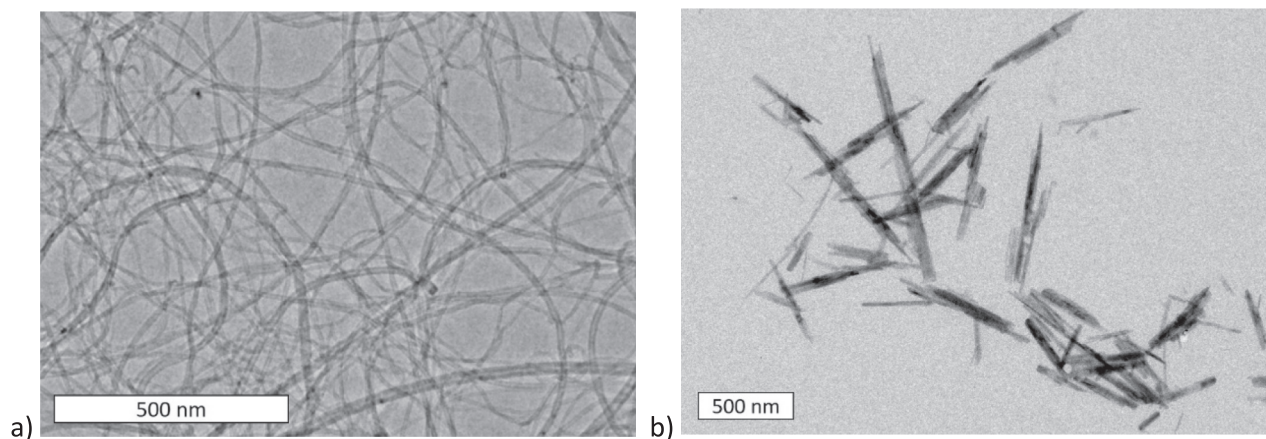


Fig.1. TEM micrographs of a) n/CNT and b) GNW nanoparticles.

Surface morphology of the prepared GNW/ n/CNT buckypapers was characterized using a Thermo Scientific Apreo C (Waltham, MA, USA) scanning electron microscope (SEM). The accelerating voltage was 2 kV, the sample was held in place by conducting carbon adhesive tape. For the characterization of the morphology, more than 100 particles were analysed using ImageJ software.

2.2.2. Characterization of wetting and evaporation

The evaporation of different solvents (5 μ L milliQ water (H_2O), methanol (MeOH), ethanol (EtOH), 2-propanol (2-PrOH), acetone (Ac) and 1,4-dioxane (1,4-Diox)) from the GNW/ n/CNT BP film was studied parallel by mass measurement, electrical resistance measurement and in case of water and ethanol, even by thermography. The films were kept at a constant 50 ± 1 °C by a purpose-built, Peltier cell-based temperature controller. The sample holder was placed on a Sartorius Cubis MSU225S-000-DU microbalance with 0.01 mg readability. The balance was linked to a data acquisition computer and the experimental data were collected by StartoCollect software during the evaporation. The sample holder plastic plate with a 0.6 cm radius gap in the centre was equipped with two copper electrical connections at the opposite edges of the gap on the bottom of the sheet. The GNW/ n/CNT BP was fixed to the bottom of the plastic section with dielectric clips. The electrical resistance of the buckypaper was measured by a Keithley 2612A Source Meter and recorded by a computer. A FLIR A655sc infrared (IR) camera was fixed vertically above the GNW/ n/CNT BP film, looking directly downwards in a direction normal to the top surface of the film. The schematics of the equipment were reported previously [44,52]. The liquid droplets (at room temperature) were instilled with Eppendorf Xplorer electronic pipette on the surface of the film, and the weight, electric resistance and temperature variation were simultaneously recorded during the evaporation process.

The FLIR A655sc IR camera has a thermal sensitivity of 30 mK, an

accuracy of ± 2 °C for temperatures up to 650 °C at 640×480 resolution. Its uncooled micro bolometer detector works in the 7.5–14.0 μ m spectral range. During the experiments, the infrared camera was equipped with a $2.9 \times (50 \mu\text{m})$ IR close-up lens, with 32×24 mm field of view and 50 μ m spatial resolution. Sessile droplet evaporation movies were recorded by FLIR Research IR software at maximum resolution with 25 Hz frame rate. The emissivity of GNW/ n/CNT BP film ($\epsilon_{\text{film}} = 0.959$) was determined by calibration at the initial film temperature (50 °C) with a FLIR tape ($\epsilon_{\text{tape}} = 0.950$). During the surface evaporation of the liquid droplets, the temperature was calculated by using the emissivity of the liquids ($\epsilon_{\text{liquid}} = 0.950$); after surface evaporation, the emissivity of the wetted film was calculated as the average between ϵ_{film} and ϵ_{liquid} [41,44,52]. The GNW/ n/CNT films were kept at 50 ± 1 °C, while the atmospheric temperature and the initial temperature of the liquid droplets were 23.7 °C and the relative humidity was 48% during the experiments. The videos and their extracted images were analysed by FLIR Research IR and ImageJ software.

3. Results

During the discussion, first the produced 1D nanomaterials were characterized, then the evaporation process was analysed based on weight and resistance measurements for the six different solvents, then we presented the process of wetting and evaporation in case of water and ethanol with the help of thermography and finally the relationships were analysed between the selected characteristic experimental parameters and the physical properties of the solvents by statistic method.

3.1. Characterization of the prepared nanoparticles

The length and diameter of the prepared carbon nanotubes and goethite nanoparticles were determined by TEM. The TEM micrographs,

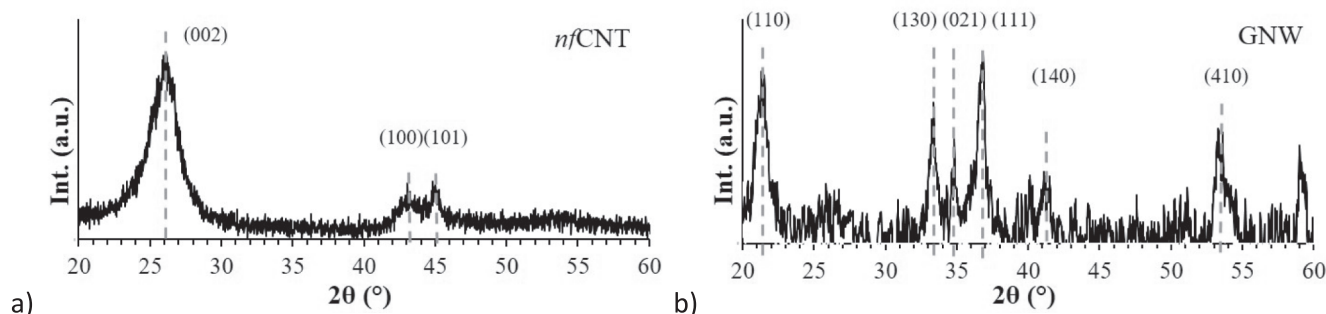


Fig.2. X-ray diffractograms of a) n/CNT and b) GNW.

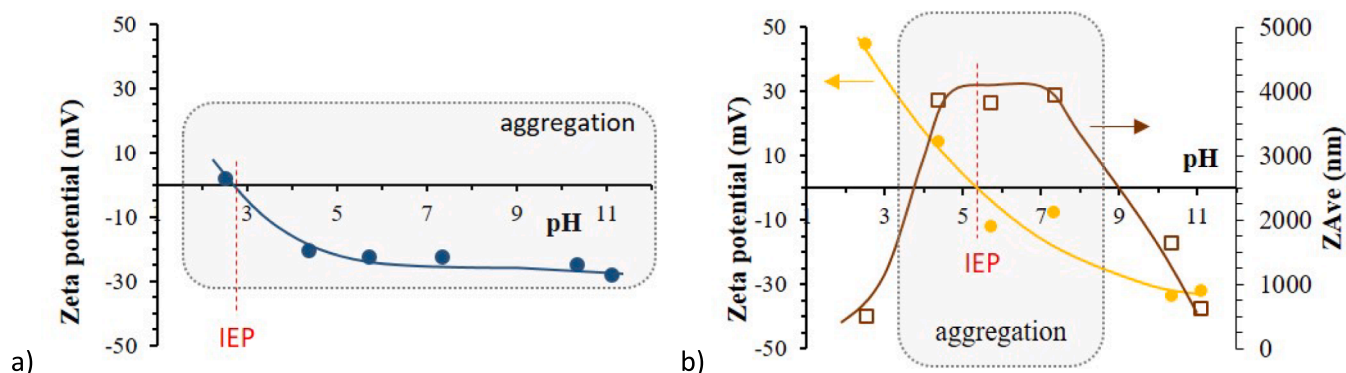


Fig. 3. Ph-dependent zeta potential and average hydrodynamic size (zave) of a) *n*/CNT and b) GNW nanoparticles (at 25 °C, 10 mmol/dm³ NaCl).

characteristic for the samples are shown in Fig. 1. The prepared carbon nanotubes were multi-wall (MWCNT), their typical length was $23.9 \pm 3.6 \mu\text{m}$, their inner diameter was $5.8 \pm 1.7 \text{ nm}$ and their outer diameter fell in the $14.1 \pm 7.5 \text{ nm}$ range as determined from TEM image analysis. The histograms are shown in the Supplementary (Fig. S1.a). The relatively wide range of the outer diameter is correlated with the variable number of the walls in the MWCNTs, which is typically 8–30 layers [57]. The goethite nanoparticles are shown in Fig. 1.b, on which the nanowire structure is clearly visible. The typical length of GNWs was $378 \pm 163 \text{ nm}$ and their diameter fell in the $38.3 \pm 19.5 \text{ nm}$ range as determined from TEM image analysis. According to the histogram shown in Supplementary (Fig. S1.b), the values of diameters have maximums close to $\sim 1 \times 23 \text{ nm}$, $\sim 2 \times 23 \text{ nm}$, $\sim 3 \times 23 \text{ nm}$ and $\sim 4 \times 23 \text{ nm}$, respectively, which suggests, that the nanowires aggregated parallel with each other during the TEM sample preparation process.

The X-ray diffractograms of the prepared *n*/CNT and goethite nanowire samples are shown in Fig. 2. The diffractogram of *n*/CNT showed the peaks at 2θ equal to 26.1° , 43.2° and 45.1° , respectively. The peaks are broad, characteristic to amorphous materials, as expected for CNTs. The multi-wall CNT (MWCNT) present characteristic peaks at $2\theta \approx 26.2^\circ$ and 43.0° , which represent the (002) and (100) planes [58]. The peak at $2\theta \approx 26.2^\circ$ indicates the presence of the effect of different overlapping graphene sheets, in a concentric mode [59], which is characteristic for the MWCNT. The peak at $2\theta \approx 45.2^\circ$ represents the (101) plane, which indicates the presence of a small amount of graphite in the sample [60]. The diffractogram of goethite nanowire is shown in Fig. 2.b. The main diffraction peaks of the GNW are located at 21.3° , 33.3° , 34.9° , 41.3° and 53.5° . This is consistent with the diffraction peak position and intensity of standard goethite (JCPDS: 00-003-0249). The determined peaks represent the (110), (130), (021), (140) and (410) planes, respectively [61]. The peaks are broad, which is expected for nanoparticles. The average crystallite size of *n*/CNT is 4.9 nm based on the Scherrer equation, which data is in good agreement with the $5.5 \pm 1.6 \text{ nm}$ published for MWCNTs prepared by CVD method. This crystallite size is notably small, much smaller than the nanotube circumference, implying that here the walls are made from a patchwork of small graphene-like grains with different orientations [62].

3.2. The surface charging and colloidal stability of *n*/CNT and GNW

The pH-dependent surface charging and aggregation of *n*/CNT and GNW nanoparticles were determined by electrokinetic potential and dynamic light scattering measurements (Fig. 3).

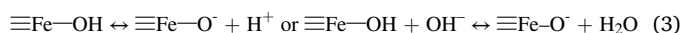
The *n*/CNT particles are not dispersible in an aqueous medium, based on the photo series shown in Supplementary (Fig. S2.a). The particles are strongly aggregated immediately after the ultrasonic treatment and these visible aggregates settle very quickly. Therefore, we did not determine the pH-dependent particle sizes for this system. The measured zeta potential values are shown in Fig. 3.a. Based on these, the *n*/CNT

particles have a pH-dependent charge state. The *n*/CNT particles are neutral at $\text{pH} \sim 2.8$, which can thus be considered the IEP of this system. IEP is the pH of isoelectric point, where the amounts of oppositely charged surface sites are equal to each other [63–65]. As the pH increases, a small amount of negative surface charge forms on the nanoparticles, indicated by electrokinetic potential $\sim -25 \text{ mV}$. In case of MWCNTs, this value suggests the trace presence of $-\text{COOH}$ functional groups [66,67]. However no pH-dependent surface charge was expected for the non-functionalized CNT, since it is assumed that there are no functional groups that can be protonated / deprotonated on its surface. Nevertheless, as a result of the used synthesis process, a small amount of $-\text{COOH}$ group can be formed on the surface of the *n*/CNT nanoparticles. The charge state of the carboxyl group is pH-dependent, in the acidic range the $-\text{COOH}$ group is in a protonated state, which is neutrally charged, and as the pH increases, the carboxyl group is continuously deprotonated, thus the negatively charged $-\text{COO}^-$ groups occurs (Eq.1.).



However, it should be noted that due to the specificity of the measurement method, the result of the electrokinetic measurements represents only a very small part of the CNT particles, since the significant part of the material has already settled as extremely large aggregates before the start of the measurement.

To understand the significant changes shown in Fig. 3.b, first the surface charging of GNW ($\alpha\text{-FeOOH}$) needs to be clarified in general. The surface of iron oxide/hydroxide/oxyhydroxide nanoparticles (INP) becomes charged, when they are dispersed in aqueous media [24,64,65,68]. Charges develop on the amphoteric surface hydroxyl groups ($\equiv\text{Fe}-\text{OH}$) and this process is controlled by both the pH and the ionic strength of aqueous medium [65,69–71]. The reactions of surface $\equiv\text{Fe}-\text{OH}$ sites with H^+ and OH^- ions lead to the formation of positive ($\equiv\text{Fe}-\text{OH}_2^+$) and negative ($\equiv\text{Fe}-\text{O}^-$) surface charges (Eqs.2,3.).



At a characteristic pH, i.e., the pH of isoelectric point (IEP), the amounts of oppositely charged surface sites are equal. At pHs lower than the IEP, the charge of INP is positive due to the presence of excess $\equiv\text{Fe}-\text{OH}_2^+$ groups, while the particles are negatively charged above the pH of IEP because of the formation of $\equiv\text{Fe}-\text{O}^-$ groups. The IEP of iron oxide/hydroxide/oxy-hydroxide particles moves in a wide range of pH, typically at $\text{pH} \sim 4.0\text{--}9.0$ [24,63]. As shown on the photo series in the Supplementary (Fig.S2.b.), after 40 min of settling, stable dispersions can be observed at pH below ~ 5 or above ~ 10 . After one day of settling, all of the particles were settled at pH above ~ 3 , which can be explained by the pH-dependent surface charges and their relatively high particle sizes ($L_{\text{GNW}} \sim 600 \text{ nm}$). According to the zeta potential values of GNW (Fig. 3.b), stable dispersion for several hours can only be prepared at pH

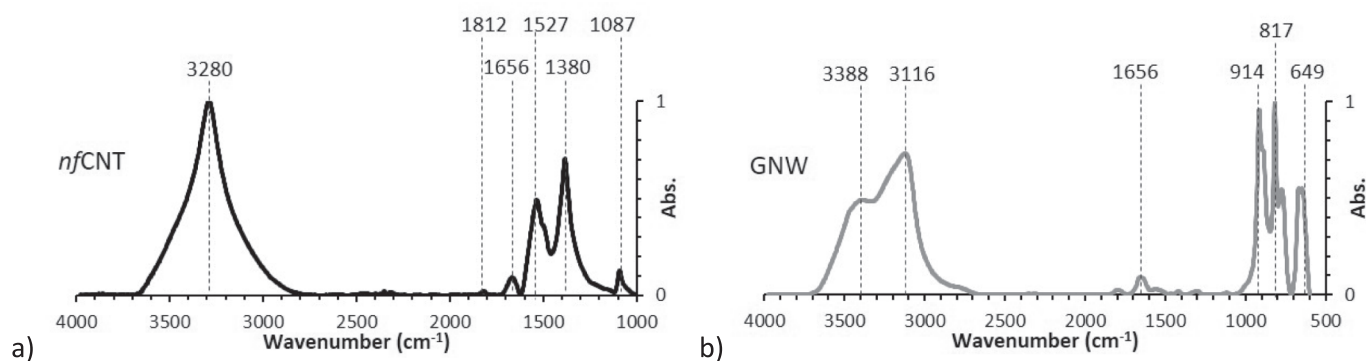


Fig. 4. ATR-FTIR spectra of a) *nfCNT* and b) GNW nanoparticles.

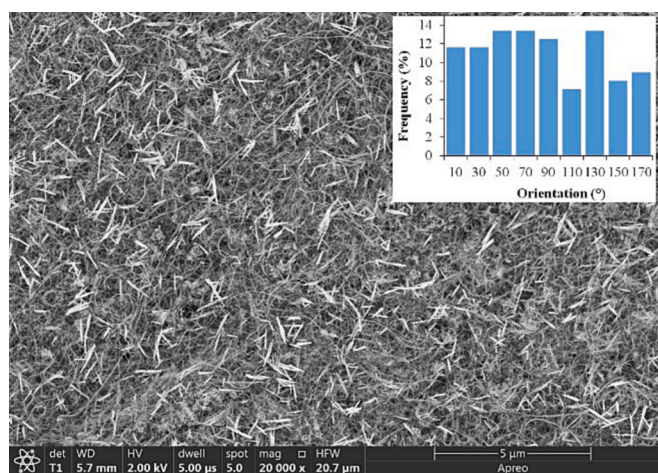


Fig. 5. SEM micrograph of GNW/*nfCNT* BP, the inserted image shown the orientation of GNW particles.

values below ~ 4 or above ~ 9 . The stable range is accompanied by a high absolute value of electrokinetic potential ($+40$ mV or -40 mV) and a relatively low hydrodynamic diameter (~ 600 nm), because of the electrostatic stabilization of particles, caused by the presence of either $\equiv\text{Fe}-\text{OH}_2^+$ in the acid range or $\equiv\text{Fe}-\text{O}^-$ surface groups in the basic range. The measured IEP of goethite nanowires, where the electrokinetic potential GNWs is zero, is at $\text{pH} \sim 5.5$. Around this pH, the GNWs are highly aggregated (the average particle size ~ 4000 nm).

ATR-FTIR analysis was used to verify the presence of the different surface functional groups, confirming our zeta potential measurement results. The IR absorption spectra of the *nfCNT* and the GNW are shown in Fig. 4. The most intensive band of the *nfCNT* is present at wavenumber 3280 cm^{-1} and can be assigned to the stretching vibrations of O—H groups. These groups can either be directly attached to the surface of the tubes or may originate from adsorbed water molecules (moisture) and carboxyl groups ($-\text{COOH}$) [67,72,73]. The characteristic band at 1527 cm^{-1} confirms the presence of aromatic C=C vibrations which are a characteristic of the carbon nanotubes structure [66,72,74]. The band at wavenumber 1380 cm^{-1} indicates the —OH groups bending vibrations [66,72]. The presence of small amounts of the carboxyl and/or

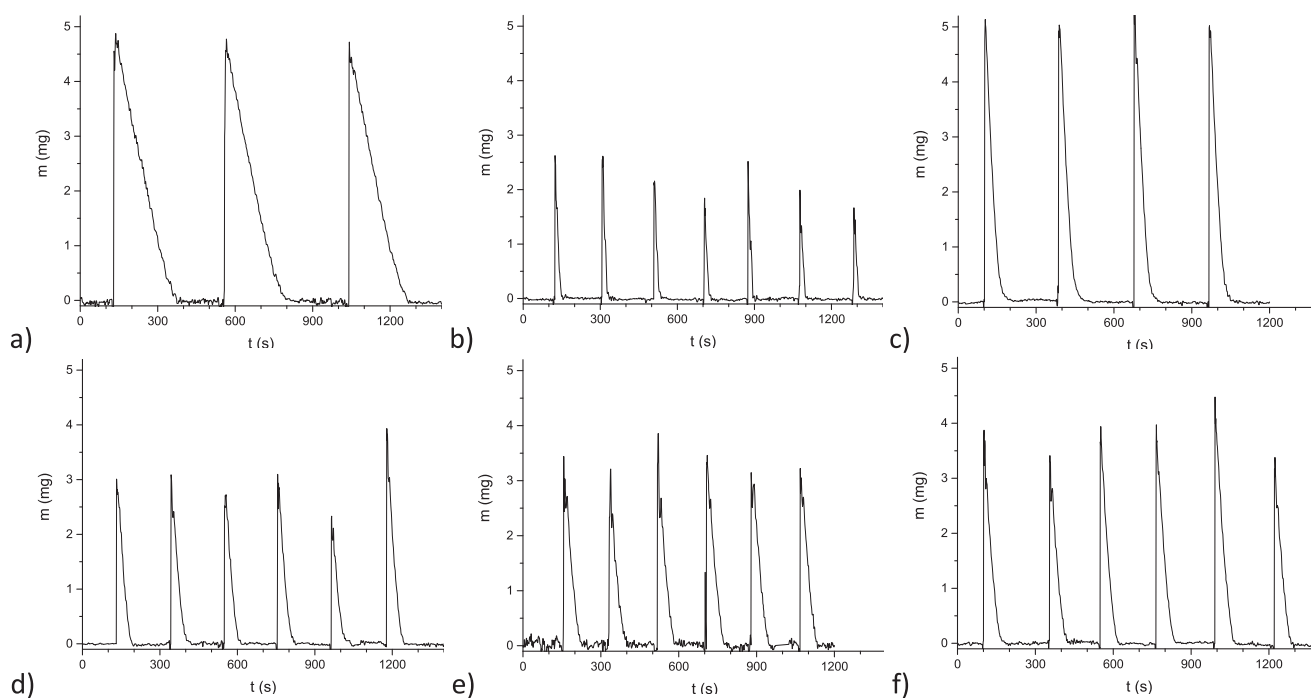


Fig. 6. Weight variation of the GNW/*nfCNT* BP as a function of time during the evaporation of different solvents (a) water, b) acetone, c) 1,4-dioxane, d) methanol, e) ethanol and f) 2-propanol). The x and y scales are the same for the easy comparison, which is $0\text{--}1400$ s on the x -axis and $0\text{--}5.5$ mg on the y -axis. ($T_{\text{solid}} = 50^\circ\text{C}$, $V_{\text{solvent}} = 5\text{ }\mu\text{L}$).

Table 1

Experimentally determined data characteristic for weight losses of the different solvent evaporations from GNW/nfCNT BP; $t_{t(m)}$ is the total evaporation time. ($T_{\text{solid}} = 50^\circ\text{C}$, $V_{\text{solvent}} = 5\ \mu\text{L}$).

		H ₂ O	MeOH	EtOH	2-PrOH	Ac	1,4-Diox
$t_{t(m)}$	s	241.0	58.2	67.5	69.0	24.0	105.0
FWHM _(m)	s	100.2	23.6	26.6	25.6	9.1	27.3
m_{max}	mg	4.8820	3.0314	3.3900	3.8427	2.4789	5.2046
dm/dt	g/s	-2.026E-05	-5.212E-05	-5.022E-05	-5.569E-05	-0.0001033	-4.957E-05

carbonyl groups can be identified by three weak bands at wavenumbers $1087\ \text{cm}^{-1}$, $1656\ \text{cm}^{-1}$ and $1812\ \text{cm}^{-1}$, which can be assigned to stretching vibrations of C—O and C=O groups [72,75]. The obtained results of FTIR analysis imply the small amounts of —OH, —C=O and —COOH groups on the surface of nfCNT [72], which thus confirms our interpretation of the measured pH-dependent surface charge results.

The IR spectrum of GNW showed three strong peaks at $649\ \text{cm}^{-1}$, $817\ \text{cm}^{-1}$ and $914\ \text{cm}^{-1}$ respectively, one weak peak at $1656\ \text{cm}^{-1}$, together with two broad bands at $3116\ \text{cm}^{-1}$ and $3388\ \text{cm}^{-1}$, which correlated well with previous reports [32,33,76,77]. The absorption bands around $3388\ \text{cm}^{-1}$ and $3116\ \text{cm}^{-1}$ are assigned to the O—H stretching vibration modes of adsorbed water and/or surface —OH groups. The weak peak at $1656\ \text{cm}^{-1}$ is assigned to the stretching vibration of —OH group on goethite. The bands at $914\ \text{cm}^{-1}$ (δOH in-plane bend) and $817\ \text{cm}^{-1}$ (γOH out-of-plane bend) which vibrate in and out respectively, are due to the Fe—OH bending vibration of goethite. The band at $649\ \text{cm}^{-1}$ can be assigned to stretching vibration of the Fe—O bond characteristic of the metal oxide [33].

3.3. The morphology of GNW/nfCNT buckypaper

The morphology of the GNW/nfCNT buckypaper was determined by SEM technique. One typical micrograph is shown in Fig. 5, where the white rod-shaped formations are the goethite nanowires, while the grey coloured loose winding formations are the carbon nanotubes. In the top-view SEM image of the composite, it is clearly visible that the carbon nanotubes rest on each other in a random arrangement, loosely, sometimes coiled and tortuous. The goethite nanowires are separated from the nfCNT fibres and the GNWs are partially found in groups (aggregated) in the composite. Based on the SEM image, the average width of the wires is $\sim 35\ \text{nm}$ and their average length is $\sim 530\ \text{nm}$, which agrees well with the TEM results. The orientation (projected on xy plane) of the

goethite nanowires was determined in the range of $0\text{--}180^\circ$, their distribution is shown in the inserted image of Fig. 5. The value of the angles is on average $\sim 85^\circ$ and the angles characterizing the orientation of the goethite nanowires are roughly evenly distributed. Based on these, the distribution of GNW in the BP can be considered random, similar to CNT nanoparticles, thus the prepared composite synthesized from nfCNT and GNW 1D nanomaterials can be called a material with a 1D random structure. The apparent pore diameter distribution characterized mostly by $40\text{--}60\ \text{nm}$ diameter pores as determined from SEM image analysis. It can be seen that the composite buckypaper is a meso/macroporous material of very similar pore structure. The porosity of the BP can be estimated from the density data of pure CNT, GNW and composite film. The calculated porosity is 90.5% , which data is in good agreement with the $89.1 \pm 1.3\%$ published for pure MWCNT BP [78].

3.4. Weight loss measurements

The evaporation of liquids can be followed by weight measurement. Droplets of different solvents were placed on the GNW/nfCNT BP and the measured weight is shown in Supplementary Fig. S3. The weight variations per solvent are shown in Fig. 6, where the \times and y scales are the same for easy comparison. The shape of the weight variation curves is characteristic to the evaporating solvents. These peaks can be characterized by their maximum value (i.e., m_{max}), full width at half maximum (FWHM), full width at base (at $m = 0\ \text{mg}$, i.e., total evaporation time, t_t) and the slope of the decline (dm/dt, i.e., average evaporation rate, v). These parameters are summarized in Table 1. The average maximum weight data (m_{max}) agrees well with the theoretical values of the $5\ \mu\text{L}$ drops' initial masses at room temperature, namely $4.99\ \text{mg}$, $3.96\ \text{mg}$, $3.95\ \text{mg}$, $3.90\ \text{mg}$, $3.95\ \text{mg}$ and $5.17\ \text{mg}$ in case of water, methanol, ethanol, 2-propanol, acetone and 1,4-dioxane, respectively. A slightly larger difference was only in the case of

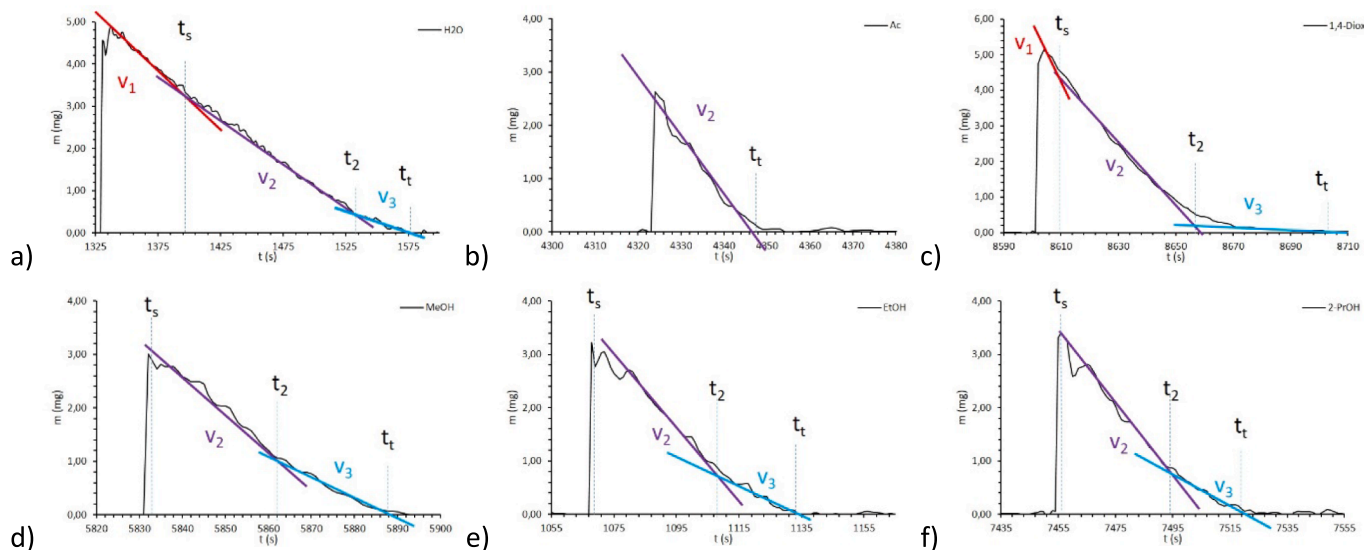


Fig. 7. Different stages for the evaporation of the solvents (a) water, b) acetone, c) 1,4-dioxane, d) methanol, e) ethanol and f) 2-propanol from the GNW/nfCNT BP sample. (v is the evaporation rate, t_s is the time of evaporation from the surface and t_t is the total evaporation time.) ($T_{\text{solid}} = 50^\circ\text{C}$, $V_{\text{solvent}} = 5\ \mu\text{L}$).

Table 2

The characteristic parameters for the divided evaporation stages determined by linear fitting on the weight variation of the GNW/nfCNT BP sample as a function of time during the vaporization of different solvents. (1st stage is evaporation from sessile droplet, 2nd stage is the vaporization of condensed liquid from porous system, 3rd stage is the evaporation of adsorbed liquid from porous system, dm/dt is the evaporation rate, t_s is the time of evaporation from the surface and t_t is the total evaporation time, m_s is the amount of liquid remaining in the pore system at t_s) ($T_{\text{solid}} = 50^\circ\text{C}$, $V_{\text{solvent}} = 5\ \mu\text{L}$).

		H ₂ O	MeOH	EtOH	2-PrOH	Ac	1,4-Diox
t_s	s	67.6					10.2
m_s	mg	3.1362					4.2695
m_s	%	64.2					82.0
dm/dt_1	g/s	-2.514E-05					-1.303E-04
t_2	s	196.9	32.3	40.4	44.2		56.5
m_2	mg	0.3978	0.9250	0.8168	0.6884		0.5337
m_2	%	8.1	30.5	24.1	17.9		10.3
dm/dt_2	g/s	-2.120E-05	-6.680E-05	-6.499E-05	-6.673E-05	-1.112E-04	-8.810E-05
t_t	s	232.6	57.6	68.7	68.4	21.2	101.2
dm/dt_3	g/s	-1.117E-05	-3.529E-05	-2.900E-05	-2.851E-05		-4.162E-06

strongly volatile solvents, which come from the measurement setup. The evaporation was the slowest ($dm/dt = -2.026\text{E-}05\text{ g/s}$, $t_t = 241\text{ s}$) in case of water and the fastest ($dm/dt = -1.033\text{E-}04\text{ g/s}$, $t_t = 24\text{ s}$) for acetone, which is consistent with our expectations. The weight decreasing is very similar for the three alcohols, which is confirmed by their characteristic parameters shown in Table 1.

The weight losses accompanying the evaporation of one drop for each solvent is shown enlarged in Fig. 7. Based on these, the evaporation can be divided into several stages in case of certain solvents, which are marked with linear sections on the graphs. In case of a porous solid material, the weight loss of the liquid measured during the evaporation can be explained by the vaporization of the sessile droplet on the solid (its rate different for a drop with contact angle (Θ) $>90^\circ$ or $<90^\circ$) and by the evaporation from the porous system (condensed or adsorbed liquid). The evaporation phenomenon can be divided into different stages, and typically, different dominant processes can be assigned to each stage [41]. The contact angle of the solvent dropped onto the GNW/nfCNT BP sample is $<90^\circ$ for all six investigated solvents. Based on these, the following three stages can probably be observed in our systems: 1)

evaporation of sessile droplet ($\Theta < 90^\circ$), 2) evaporation of condensed liquid from the porous system and 3) the evaporation of the adsorbed liquid molecules.

The evaporation rate (dm/dt) for the divided vaporization stages were determined by linear fitting as reported in Table 2. The characteristic values of the first stage are the end of the stage as well, which is the end of evaporation from the surface (t_s), and the amount of liquid remaining in the pore system at t_s (m_s , which can be given in absolute value and in relation to the initial mass of the liquid). The second stage, similar to the first, can be characterized by the t_2 value indicating the end of the stage and the absolute and relative mass of the liquid (m_2) remaining in the solid sample. The end of the third stage equals the end of the entire evaporation process (total evaporation time, t_t). All these data can be found in Table 2.

In case of water and 1,4-dioxane, all three stages can be determined, because the measurable part of the liquid remains long enough in the sessile droplet on top of the solid sample (t_s (H₂O) $\sim 68\text{ s}$, t_s (1,4-Diox) $\sim 10\text{ s}$) and additionally the entire evaporation process is long enough for the assessment (t_t (H₂O) $\sim 233\text{ s}$, t_t (1,4-Diox) $\sim 101\text{ s}$). The alcohols

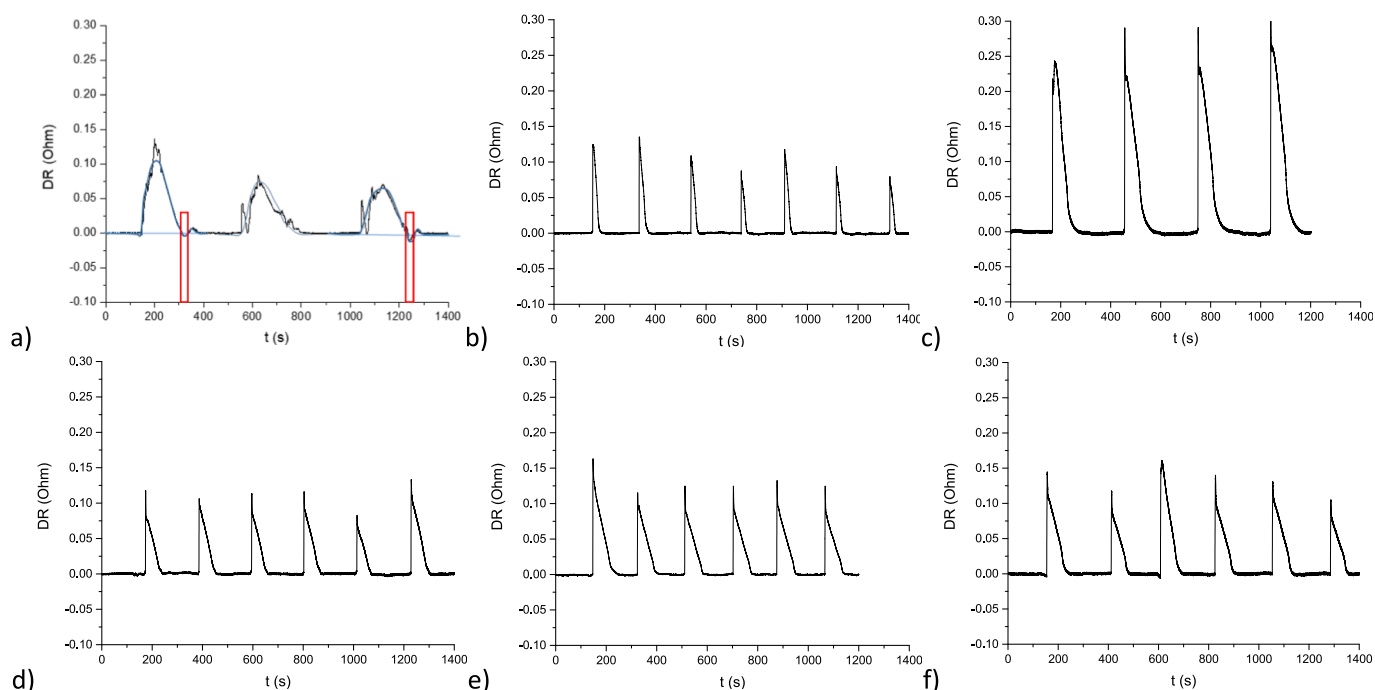


Fig. 8. Electrical resistance variation (DR) of the GNW/nfCNT BP as a function of time during the evaporation of different solvents (a) water, b) acetone, c) 1,4-dioxane, d) methanol, e) ethanol and f) 2-propanol). The \times and y scales are the same for the easy comparison, which is 0 – 1400 s on the x-axis and $-0.1 - 0.3$ Ohm on the y-axis. For better visibility, the shapes of the typical signal have been drawn by hand on the graph of the water, and the characteristic parts of the curves are signed by rectangles. ($T_{\text{solid}} = 50^\circ\text{C}$, $V_{\text{solvent}} = 5\ \mu\text{L}$).

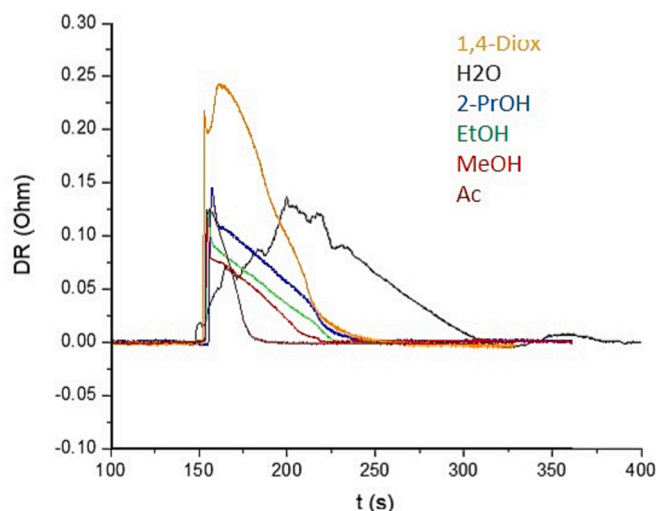


Fig. 9. Enlarged peaks of the electrical resistance variation as a function of time (evaporation profile) for the vaporization of different solvents from the GNW/nfCNT BP sample. ($T_{\text{solid}} = 50\text{ }^{\circ}\text{C}$, $V_{\text{solvent}} = 5\text{ }\mu\text{L}$).

immediately disappear from the surface of the GNW/nfCNT BP sample, so we can only use the 2nd and 3rd stages to interpret their evaporation processes. With this analysis method, the signals of methanol, ethanol and 2-propanol can be better separated from each other. The vaporization of acetone is so fast ($t_{\text{t}}(\text{Ac}) \sim 20\text{ s}$) that only one stage can be determined, which is assumed to be the 2nd stage.

Based on the results we can conclude, that i) the evaporation rate for the divided stages of the evaporation is constant with a good approximation, ii) the evaporation rate decreases systematically in the successive stages (see in Supplementary Fig. S4), and iii) with this more detailed analysis, signs of alcohols with similar properties can be better distinguished from each other.

3.5. Electrical resistance measurements

The vaporization of solvents was followed by electrical resistance measurement. Droplets of different solvents were placed on the GNW/nfCNT BP and the measured electrical resistance is shown in Supplementary Fig.S5. The electrical resistance variations per solvent are shown in Fig. 8, where the \times and y scales are the same for easy comparison.

The shapes of the electrical resistance variation curves are characteristic for the evaporating solvents. In case of organic solvents, the shape of the curve is simple, it quickly reaches its maximum after the liquid drop addition, from where the value of the electrical resistance continuously decreases back to the base line until the end of the evaporation. The electrical resistance variation is very similar for the three alcohols. In case of a water drop, the change in electrical resistance is much more complex, the value of R increases continuously after the addition of the drop, and then begins to decrease after its maximum. The value of the electrical resistance drops below the baseline, then rises again after its minimum and returns back to the baseline until the end of

the vaporization. This behaviour is well known from our previous measurements in the case of pure nfCNT BP - water system. The electrical resistance measuring that is part of our experimental setup measures with greater uncertainty in case of water, which we could not managed to solve yet. Despite the poor quality of the electrical resistance measurement in the case of GNW/nfCNT BP - water system, we performed the evaluation based on our earlier results for nfCNT BP. For better visibility, the shapes of the typical signal have been drawn by hand on the graph of the water in Fig. 8.a, and the characteristic parts of the curves are signalled by rectangles.

The electrical resistance variation accompanying the evaporation of one drop for each solvent is shown enlarged in Fig. 9. According to this, the shape of peaks is unique for the evaporating solvents. The fine details of the shape of the curve (maximum value, time to reach the maximum, full width at half maximum, full width at the base, area, shape of the tail etc.) are slightly different for every solvent. A new terminology was introduced for this, the electrical resistance (R) as a function of time (t) is termed as the “evaporation profile” (EP) of the solvent [44]. After the analysis, the peaks were characterized by their maximum (maximum value is ΔR_{max} and the time to reach the maximum is t_{s}), full width at half maximum (FWHM), full width at base (at $\Delta R = 0\text{ Ohm}$, i.e., total evaporation time, t_{t}) and the area under peak (Area). These parameters are summarized in Table 3.

The total evaporation times ($t_{\text{t(R)}}$) obtained from the evaluation of the evaporation profile are consistent with the values obtained from the mass measurement ($t_{\text{t(m)}}$). In case of organic solvents, the $t_{\text{t(R)}}$ values are slightly ($\sim 8\%$) higher than the $t_{\text{t(m)}}$ values, which may be due to the higher accuracy of the electrical resistance measurement. Probably a trace amount of residual solvent, which is no longer detectable by the balance, still has a measurable effect on the electrical resistance value. From the evaluation of the evaporation profile, we can determine the surface evaporation time ($t_{\text{s(R)}}$) for all solvents, which in case of water and 1,4-dioxane matches well with the $t_{\text{s(m)}}$ values calculated from the detailed evaluation of the weight measurement. The $t_{\text{s(R)}}$ value of alcohols and acetone is $\sim 1\text{--}2\text{ s}$, i.e. after the drop addition, a sessile droplet is found on the surface of the solid sample only for a very short time, the solvent quickly evaporating and/or entering the pore system. This is in accordance with the stages of the evaporation determined from the weight measurements. 1,4-dioxane showed the largest electrical resistance change ($\Delta R_{\text{max}} = 0.285\text{ Ohm}$) and water showed the smallest change ($\Delta R_{\text{max}} = 0.097\text{ Ohm}$), which can be explained by their electrical conductivity. During the evaluation of the water's evaporation profile, the negative peaks were also fitted ($\text{FWHM}_{2(\text{R})} = 13.6\text{ s}$, $\Delta R_{\text{min}} = -0.0108\text{ Ohm}$, $\text{Area}_2 = -0.2335\text{ Ohm}\cdot\text{s}$). The width of the positive peak is 169.8 s , and the width of the negative peak is 33.8 s . The area under the negative peak is only $\sim 2\%$ of the total area under the curve, but this is characteristic to the water evaporation. The experimental parameters determined for alcohols show small differences.

Statistical methods (e.g., Pearson correlation coefficients) can be used in order to specify the relationship between the selected characteristic experimental parameters and the physical properties of the solvents (see 3.7 Section).

Table 3

Characteristic parameters of the evaporation profiles (electric resistance as a function of time) for the different solvent evaporations from GNW/nfCNT BP; $t_{\text{t(R)}}$ is the total evaporation time, $t_{\text{s(R)}}$ is the time of evaporation from the surface. ($T_{\text{solid}} = 50\text{ }^{\circ}\text{C}$, $V_{\text{solvent}} = 5\text{ }\mu\text{L}$).

		H ₂ O	MeOH	EtOH	2-PrOH	Ac	1,4-Diox
$t_{\text{t(R)}}$	s	242.0	65.2	76.8	73.2	27.2	109.6
$t_{\text{s(R)}}$	s	65.8	1.7	1.4	2.1	0.9	9.1
$\text{FWHM}_{2(\text{R})}$	s	85.8	25.5	25.8	28.7	14.2	40.1
ΔR_{max}	Ohm	0.0969	0.1117	0.1244	0.1278	0.1020	0.2845
Area	Ohm·s	8.9946	2.9997	3.6364	4.0109	1.4678	11.4773

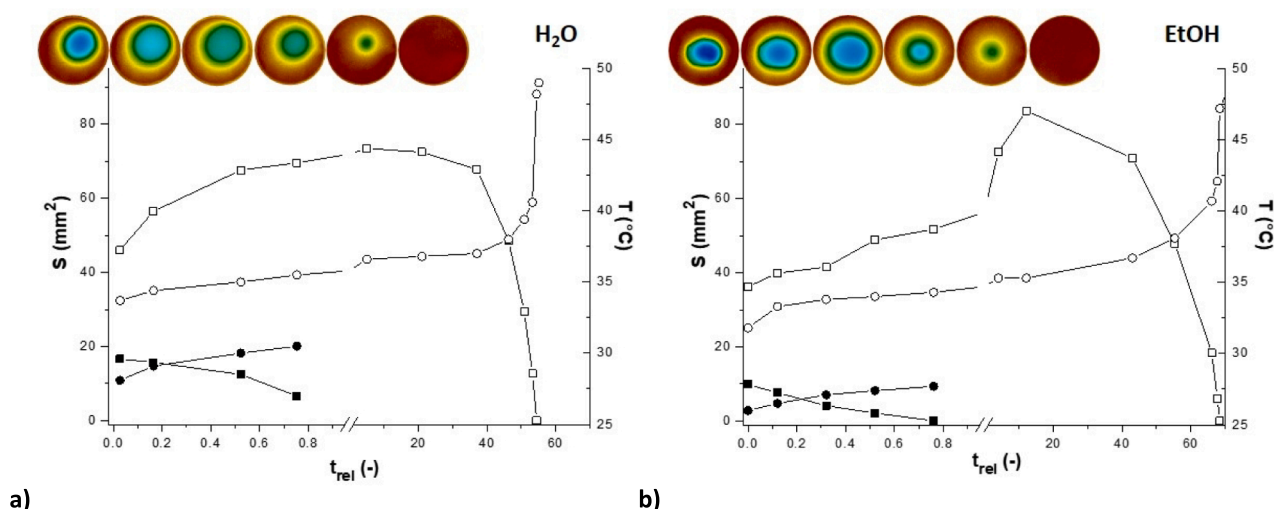


Fig.10. The variation of the area (S) and average temperature (T) of the sessile droplet on surface (d) and of the wetted region (w) as a function of relative time (t/t_s) during the evaporation of a) water and b) ethanol from GNW/nfCNT BP sample. The images in the upper left corners (exported pro rata from the IR video) correspond to initial moments of evaporation (t_0), total surface evaporation (t_s), three representative intermediate time and end of the vaporization (t_t), respectively. ($T_{\text{solid}} = 50^\circ\text{C}$, $V_{\text{solvent}} = 5\ \mu\text{L}$).

Table 4

Data extracted from infrared videos characteristic for the evaporation of water and ethanol from GNW/nfCNT BP sample. $S_{d(t_0)}$ is the initial area of the drops, $S_{w(t_0)}$ and $S_{w(t_s)}$ are the areas of the wetted region at t_0 and at the end of the surface evaporation (t_s), t_t is the total evaporation time, $R_{d,\text{max}}$ and $R_{w,\text{max}}$ are the maximum radius of the sessile droplet and wetted area. ($T_{\text{solid}} = 50^\circ\text{C}$, $V_{\text{solvent}} = 5\ \mu\text{L}$).

	$S_{d(t_0)}$ mm^2	$S_{w(t_0)}$ mm^2	$S_{w(t_s)}$ mm^2	t_s s	t_t s	$R_{d,\text{max}}$ mm	$R_{w,\text{max}}$ mm
H ₂ O	16.64	46.02	71.88	61.2	237.6	2.30	4.84
EtOH	9.86	36.20	56.25	1.0	68.4	1.77	5.16

3.6. Measurements by infrared camera

Infrared imaging was used to monitor the evaporation of water and ethanol from the GNW/nfCNT BP sample from a vertical perspective. The water and ethanol were selected as representative members of the two solvents' groups based on weight and electrical measurements showing different characteristic behaviour. The videos were evaluated at selected representative moments. In Fig. 10 the determined spot area and average temperature of the sessile droplet (S_d , T_d) and of the wetted region (S_w , T_w) are plotted as a function of relative time ($t_{\text{rel}} = t/t_s$). At the end of the surface vaporization (t_s) S_d is 0 and t_{rel} is 1. The evaluated data characteristic for the evaporation of the liquids are reported in Table 4.

The characteristic spot area values obtained for water were in all cases higher than the values obtained for ethanol. Examined on the same relative time scale, in the first evaporation stage (evaporation of the sessile droplet) the area of the sessile drops was typically 1.7 times, while the area of the wetted region was 1.3 times bigger in case of water (see Table 4). During the evaporation of the sessile droplets of water and ethanol, their S_d values were decreasing and their averaged T_d values were increasing continuously. The t_s values ($t_{s(\text{IR}),\text{EtOH}} = 1.0\ \text{s}$ and $t_{s(\text{IR}),\text{H}_2\text{O}} = 61.2\ \text{s}$) match well with the values determined from the electrical resistances measurements.

At the beginning of the experiments (t_0) some part of the liquid immediately enters the pore system. The wetted area of water is approximately 2.8 times the area of its sessile droplet, while this ratio for ethanol is 3.6. In the first evaporation range the wetted area increases continuously for both solvents. The $S_{w(t_s)}$ value is approximately 1.6 times the $S_{w(t_0)}$ value for both water and alcohol. This indicates that the

solvent continuously diffuses into the pore system from the sessile droplet on the surface, and the liquid reaches and wets a larger and larger area in the porous system of the solid sample. After the disappearance of the sessile droplet, the second vaporization stage begins, when the fluid evaporates from the porous system. During this range, the wetted area of the water barely increases, and then begins to decrease after a roughly constant period. In case of ethanol, even after the disappearance of the sessile droplet, the wetted area still increases definitely, its maximum value ($S_{w,\text{max},\text{EtOH}} = 83.60\ \text{mm}^2$) being approximately 2.3 times the initial value, after which the wetted area starts to decrease rapidly down to $S_w = 0\ \text{mm}^2$ at the total evaporation time (t_t). Based on all this, ethanol wets the GNW/nfCNT BP sample much better. The t_t values ($t_{t(\text{IR}),\text{EtOH}} = 68.4\ \text{s}$ and $t_{t(\text{IR}),\text{H}_2\text{O}} = 237.6\ \text{s}$) correspond well with the values determined from the weight and electrical resistances measurements.

Before the thermography experiments, liquids were kept at room temperature ($T = 23.7^\circ\text{C}$) to improve the infrared contrast. Therefore, there was a temperature difference between the initial $5\ \mu\text{L}$ drops and the GNW/nfCNT BP sample kept at 50°C . The temperature of the solvents and the solid was changing continuously during the experiment because of the initial difference, the heating of the solid sample, the endotherm vaporization process, etc. The temperature change profile is characteristic for the measured solvent. The variations of average temperature for the drop (T_d) and wetted region (T_w) were plotted as a function of relative time in Fig. 10. The T_d and T_w values increase continuously, but there is a longer, almost constant temperature period for water and ethanol as well. The temperature variation along with the radius of the GNW/nfCNT BP for the vaporization of water and ethanol is represented at some characteristic moment (e.g., t_0 , t_s , t_t) in Supplementary (Fig. S6). By analysing these, it is possible to monitor the warming of the sessile droplet (red arrows with continuous line) and the spread and warming of the liquid in the pore system (red arrows with dotted line) during the first evaporation stage, as well as the changes of the wetted region during the second and third evaporation states (vaporization from the porous system) signed by blue arrows.

3.7. Analysis of the characteristic experimental parameters

It is intriguing to uncover relationships between the physical properties of the studied liquids (water, methanol, ethanol, 2-propanol, acetone, 1,4-dioxane) and the experimentally determined data of the evaporation from the GNW/nfCNT BP sample. For the characterization

Table 5

Pearson correlation coefficient (PCC) matrix for the specific evaporation parameters of the GNW/nfCNT BP sample and the physical properties of studied solvents. ($T_{\text{solid}} = 50^\circ\text{C}$, $V_{\text{solvent}} = 5\ \mu\text{L}$) (Highlighted in light blue: moderate correlation, in cyan blue: high correlation, in dark blue: very high correlation.) Total evaporation time: t_t , time of evaporation from the surface: t_s , time of the end of the second vaporization stage determined from weight measurements: t_2 , averaged studied amount of fluids: m_{max} , weight of the liquid remaining in the solid sample at t_2 : m_2 , averaged evaporation rate: dm/dt , evaporation rate during the 2nd evaporation range: v_2 , evaporation rate during the 3rd evaporation range: v_3 , full width at half maximum from weight and electric resistance measurements: $\text{FWHM}_{(m)}$ and $\text{FWHM}_{(R)}$, maximum of the electrical resistance change: ΔR_{max} , averaged area under peak from electric resistance measurements: $\text{Area}_{(R)}$, molecular mass: M , density: ρ , viscosity: η , melting point: T_{melting} , boiling point: T_{boiling} , standard enthalpy change of vaporization: $\Delta_{\text{vap}}H^\ominus$, heat capacity: c_p , surface tension: γ , dipole moment: D , acid dissociation constant: pK_a , dielectric constant: ϵ .

	t_t	t_s	t_2	m_{max}	m_2	dm/dt	v_2	v_3	$\text{FWHM}_{(m)}$	$\text{FWHM}_{(R)}$	ΔR_{max}	$\text{Area}_{(R)}$
M	-0.466	-0.570	-0.538	0.186	-0.064	0.419	-0.722	0.375	-0.617	-0.470	0.807	0.254
ρ	-0.449	-0.239	0.617	-0.611	-0.856	0.878	-0.679	0.971	-0.397	-0.432	-0.270	-0.497
η	0.120	-0.051	-0.190	0.476	-0.208	-0.376	0.252	0.061	0.057	0.109	0.294	0.289
T_{melt}	0.272	0.226	0.094	0.254	0.071	-0.401	0.260	0.073	0.235	0.291	0.193	0.338
T_{boil}	0.772	0.608	0.636	0.985	-0.958	-0.781	0.563	0.957	0.651	0.760	0.541	0.929
$\Delta_{\text{vap}}H^\ominus$	0.582	0.433	0.492	0.557	-0.392	-0.847	0.824	-0.019	0.584	0.564	-0.048	0.363
c_p	-0.453	-0.543	-0.493	0.132	-0.093	0.416	-0.618	0.246	-0.569	-0.457	0.605	0.116
γ	0.971	0.992	0.985	0.639	-0.808	-0.673	0.742	0.613	0.965	0.976	-0.089	0.625
D	-0.246	-0.008	0.266	-0.766	0.262	0.566	-0.164	-0.650	-0.084	-0.233	-0.840	-0.770
pK_a	-0.233	-0.059	0.042	-0.762	0.433	0.308	0.098	-0.791	-0.044	-0.228	-0.962	-0.855
ϵ	0.772	0.860	0.847	0.164	-0.369	-0.572	0.831	0.043	0.877	0.775	-0.617	0.101

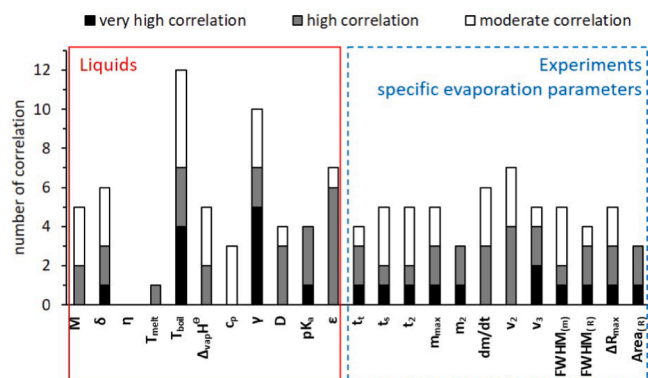


Fig. 11. The number of different correlation types for physical properties of studied liquids and the specific evaporation parameters of the GNW/nfCNT BP sample. Data come from the PCC matrix in Table 5.

of the solvents, the following data were used, collected from widely accepted reference sources: molecular mass: M , density: ρ , viscosity: η , melting point: T_{melting} , boiling point: T_{boiling} , standard enthalpy change of vaporization: $\Delta_{\text{vap}}H^\ominus$, heat capacity: c_p , surface tension: γ , dipole moment: D , acid dissociation constant: pK_a , dielectric constant: ϵ . For the studied liquids, the characteristic measured data are the total evaporation time: t_t , time of evaporation from the surface: t_s , time of the end of the second vaporization stage determined from weight measurements: t_2 , averaged studied amount of fluids: m_{max} , weight of the liquid remaining in the solid sample at t_2 : m_2 , averaged evaporation rate: dm/dt , evaporation rate during the 2nd evaporation range: v_2 , evaporation rate during the 3rd evaporation range: v_3 , full width at half maximum from weight and electric resistance measurements: $\text{FWHM}_{(m)}$ and $\text{FWHM}_{(R)}$, maximum of the electrical resistance change: ΔR_{max} , averaged area under peak from electric resistance measurements: $\text{Area}_{(R)}$. All these data are summarized in the Supplementary Table S1.

To analyse this dataset, the matrix of Pearson correlation coefficients (PCC) was used. It is essential to focus on the correlations between one measured value and one chosen physical property to uncover the relationships between experimentally determined data and the properties

of solvents as defined by their physical properties. These PCC data are listed in Table 5 as the relevant part of the PCC matrix. The correlation between two chosen parameters is positive when the values increase together, and negative when one value decreases as the other increases. The absolute magnitude of coefficient is proportional to the strength of correlation. The characteristic ranges of PCC values are not unambiguously agreed on in the literature [79,80]. The ranges used in the present study are the following: 0.00 to 0.30 indicates negligible correlation, 0.30 to 0.50 is low correlation, 0.50 to 0.70 signifies moderate correlation (highlighted in light blue in Table 5), 0.70 to 0.90 means high correlation (highlighted in cyan blue) and 0.90 to 1.00 signals very high correlation (highlighted in dark blue) [41].

Moderate, high or very high correlation ($0.5 < |\text{PCC}| < 1.0$) were observed in 43 % of the examined cases. This confirms that the chosen characteristic values are suitable for PCC testing. High correlation ($0.7 < |\text{PCC}| < 0.9$) and very high correlation ($0.9 < |\text{PCC}| < 1.0$) were observed in 18 % and 8% of the examined cases. The number of different correlation types for physical or experimental parameters is shown in Fig. 11. Among the physical properties of the studied liquids, the boiling point and surface tension have the most dominant relationship with the experimentally determined specific evaporation parameters. The main part of the experimental data has at least one very high and one or two high correlations with the physical properties of the solvents. The relationships presented in Table 5 allow us to estimate the physical parameters of the solvents, and thus obtain qualitative information for an unknown liquid based on the experimental results determined by our method. For example, it is possible to estimate the surface tension from t_t ($\text{PCC} = 0.971$) or t_s ($\text{PCC} = 0.992$), the boiling point from $\text{Area}_{(R)}$ ($\text{PCC} = 0.929$), the pK_a from ΔR_{max} ($\text{PCC} = -0.962$) or the: $\Delta_{\text{vap}}H^\ominus$ from dm/dt ($\text{PCC} = -0.847$).

4. Summary

Non-functionalized carbon nanotube based buckypaper doped by 10 wt% goethite nanowire (GNW/nfCNT BP) was synthesized by dead-end filtration technique, the composite is a material with 1D random nanostructure. The wetting and evaporation of GNW/nfCNT BP were characterized in case of six solvents by different techniques.

The weight reduction accompanying vaporization was monitored.

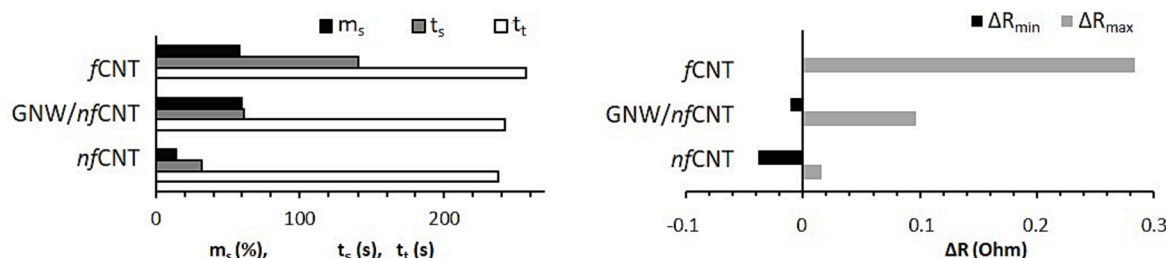


Fig. 12. Some characteristic experimental data for the evaporation of water from the GNW/nfCNT BP compared to the pure nfCNT and pure fCNT BP samples [52]. ($T_{solid} = 50$ °C, $V_{solvent} = 5$ μ L) (Total evaporation time: t_t , time of evaporation from the surface: t_s , weight of the liquid remaining in the solid sample at t_s , m_s , maximum and minimum of the electrical resistance changes: ΔR_{max} , ΔR_{min}).

Based on its analysis, the evaporation process of the solvents from porous material can be divided into three stages (evaporation of the sessile droplet, the condensed and adsorbed liquid from the porous system). The amount of remaining liquid in the solid sample at t_s and t_t can be determined, the latter can presumably be identified as adsorbed solvent. The evaporation rate for the divided stages of the vaporization is constant with a good approximation, and they systematically decrease in the successive stages. During the electrical resistance measurements, we characterized our systems using the evaporation profile. Water showed a completely different behaviour compared to organic solvents. The liquids could be distinguished from each other, e.g. by the value of the t_t and the $Area_{(R)}$. The wetting process can be observed with thermography. The area of the sessile droplet on the top of the sample and of the wetted pore system can be distinguished at a given time. The change in the wetted area effectively characterizes the extent to which the liquid wets the studied porous material.

Based on the PCC analysis, in some cases a very strong correlation can be observed, thus it is possible to estimate, e.g. the surface tension from t_t (PCC = 0.971), t_s (PCC = 0.992) or FWHM $_{(R)}$ (PCC = 0.976), the boiling point from $Area_{(R)}$ (PCC = 0.929), the pK_a from ΔR_{max} (PCC = -0.962) and the $\Delta_{vap}H^\ominus$ from dm/dt (PCC = -0.847). These results allow us to predict the possibility of this experimental setup and analysis method in a potential future analytical application. Some characteristic experimental data of the examined GNW doped nfCNT BP are shown in Fig. 12, together with the data of the non-functionalized and the functionalized carbon nanotube buckypaper samples (nf- and fCNT) [52]. The properties of the composite BP fall between those of pure nfCNT and fCNT BPs. This provides an opportunity to fine-tune the surface properties of the BPs by simply varying the added amount of hydrophilic goethite nanowire. Moreover, the potential application of goethite nanomaterials in water purification offers the opportunity of further investigation of this GNW/nfCNT BP composite in this fundamentally important direction as well.

CRedit authorship contribution statement

Ildikó Y. Tóth: Investigation, Formal analysis, Visualization, Conceptualization, Supervision, Writing – original draft, Writing – review & editing. **Gábor Veress:** Investigation, Formal analysis. **Imre Szenti:** Investigation. **Ákos Kukovecz:** Conceptualization, Funding acquisition.

Declaration of Competing Interest

The authors declare that they have no known competing financial interests or personal relationships that could have appeared to influence the work reported in this paper.

Data availability

Data will be made available on request.

Acknowledgement

I.Y. Toth acknowledge the support by the **János Bolyai Research Scholarship** of the Hungarian Academy of Sciences and the Ministry of Human Capacities, Hungary through the grant **ÚNKP-19-4 New National Excellence Program**. Project no. RRF-2.3.1-21-2022-00009, titled National Laboratory for Renewable Energy, has been implemented with the support provided by the Recovery and Resilience Facility of the European Union within the framework of Programme Széchenyi Plan Plus. Project no. **TKP2021-NVA-19** has been implemented with the support provided by the Ministry of Innovation and Technology of Hungary from the National Research, Development and Innovation Fund, financed under the TKP2021-NVA funding scheme.

References

- [1] A. Acharya, P.K. Pal, Agriculture nanotechnology: translating research outcome to field applications by influencing environmental sustainability, *NanoImpact* 19 (2020), 100232, <https://doi.org/10.1016/j.nimpact.2020.100232>.
- [2] U. Banin, N. Waiskopf, L. Hammarström, G. Boschloo, M. Freitag, E.M. J. Johansson, J. Sá, H. Tian, M.B. Johnston, L.M. Herz, R.L. Milot, M.G. Kanatzidis, W. Ke, I. Spanopoulos, K.L. Kohlstedt, G.C. Schatz, N. Lewis, T. Meyer, A.J. Nozik, M.C. Beard, F. Armstrong, C.F. Megarity, C.A. Schmittenmaier, V.S. Batista, G. W. Brudvig, *Nanotechnology for catalysis and solar energy conversion*, *Nanotechnology* 32 (2021), 042003, <https://doi.org/10.1088/1361-6528/abce8>.
- [3] Z. Fattahi, M. Hasanazadeh, Nanotechnology-assisted microfluidic systems for chemical sensing, biosensing, and bioanalysis, *TrAC Trends Anal. Chem.* 152 (2022), 116637, <https://doi.org/10.1016/j.trac.2022.116637>.
- [4] G. Cheraghian, S. Rostami, M. Afrand, Nanotechnology in Enhanced Oil Recovery, *Processes* 8 (2020) 1073, <https://doi.org/10.3390/pr8091073>.
- [5] X. Jiang, C. Bai, M. Liu, *Nanotechnology for microfluidics*, Wiley-VCH, 2019.
- [6] N. Rabiee, S. Ahmadi, Y. Fatahi, M. Rabiee, M. Bagherzadeh, R. Dinarvand, B. Bagheri, P. Zarrintaj, M.R. Saeb, T.J. Webster, Nanotechnology-assisted microfluidic systems: from bench to bedside, *Nanomedicine* 16 (2021) 237–258, <https://doi.org/10.2217/nmm-2020-0353>.
- [7] M.Y. Rezk, N.K. Allam, Impact of nanotechnology on enhanced oil recovery: a mini-review, *Ind. Eng. Chem. Res.* 58 (2019) 16287–16295, <https://doi.org/10.1021/acs.iecr.9b03693>.
- [8] X. Fang, B. Li, E. Petersen, Y.S. Seo, V.A. Samuilov, Y. Chen, J.C. Sokolov, C. Y. Shew, M.H. Rafailovich, Drying of DNA droplets, *Langmuir* 22 (2006) 6308–6312, <https://doi.org/10.1021/la060479u>.
- [9] J. He, Q. Zhang, S. Gupta, T. Emrick, T.R. Russell, P. Thiyagarajan, Drying droplets: a window into the behavior of nanorods at interfaces, *Small* 3 (2007) 1214–1217, <https://doi.org/10.1002/sml.200700055>.
- [10] M. Singh, H.M. Haverinen, P. Dhagat, G.E. Jabbour, Inkjet printing-process and its applications, *Adv. Mater.* 22 (2010) 673–685, <https://doi.org/10.1002/adma.200901141>.
- [11] N. Gupta, S.M. Gupta, S.K. Sharma, Carbon nanotubes: synthesis, properties and engineering applications, *Carbon Lett.* 29 (2019) 419–447, <https://doi.org/10.1007/s42823-019-00068-2>.
- [12] M.N. Norizan, M.H. Moklis, S.Z.N. Demon, N.A. Halim, A. Samsuri, I.S. Mohamad, V.F. Knight, N. Abdullah, Carbon nanotubes: functionalisation and their application in chemical sensors, *RSC Adv.* 10 (2020) 43704–43732, <https://doi.org/10.1039/D0RA09438B>.
- [13] N. Anzar, R. Hasan, M. Tyagi, N. Yadav, J. Narang, Carbon nanotube - A review on synthesis, properties and plethora of applications in the field of biomedical science, *Sensors Int.* 1 (2020), 100003, <https://doi.org/10.1016/j.sintl.2020.100003>.
- [14] S. Rathinavel, K. Priyadarshini, D. Panda, A review on carbon nanotube: an overview of synthesis, properties, functionalization, characterization, and the application, *Mater. Sci. Eng. B* 268 (2021), 115095, <https://doi.org/10.1016/j.mseb.2021.115095>.

- [15] R. Shoukat, M.I. Khan, Carbon nanotubes: a review on properties, synthesis methods and applications in micro and nanotechnology, *Microsyst. Technol.* 27 (2021) 4183–4192, <https://doi.org/10.1007/s00542-021-05211-6>.
- [16] P. Zhang, J. Su, J. Guo, S. Hu, Influence of carbon nanotube on properties of concrete: a review, *Constr. Build. Mater.* 369 (2023), 130388, <https://doi.org/10.1016/j.conbuildmat.2023.130388>.
- [17] K. Pyrzyńska, Recent applications of carbon nanotubes for separation and enrichment of lead ions, *Separations* 10 (2023) 152, <https://doi.org/10.3390/separations10030152>.
- [18] A. Cadena, B. Botka, K. Kamarás, Organic molecules encapsulated in single-walled carbon nanotubes, *Oxford Open Mater. Sci.* 1 (2021), itab009, <https://doi.org/10.1093/oxfmat/itab009>.
- [19] N.A. Prokudina, E.R. Shishchenko, O.S. Joo, K.H. Hyung, S.H. Han, A carbon nanotube film as a radio frequency filter, *Carbon* 43 (2005) 1815–1819, <https://doi.org/10.1016/j.carbon.2005.02.012>.
- [20] U. Vohrer, I. Kolaric, M.H. Haque, S. Roth, U. Detlaff-Weglikowska, Carbon nanotube sheets for the use as artificial muscles, *Carbon* 42 (2004) 1159–1164, <https://doi.org/10.1016/j.carbon.2003.12.044>.
- [21] D. Prasad, L. Zhiling, N. Satish, E.V. Barrera, Nanotube film based on single-wall carbon nanotubes for strain sensing, *Nanotechnology* 15 (2004) 379, <https://doi.org/10.1088/0957-4848/15/3/026>.
- [22] P.K. Vishwakarma, S.K. Pandey, A.K. Singh, S. Rathore, K. Ram, R. Giri, A. Srivastava, Reusable and thermostable multiwalled carbon nanotubes membrane for efficient removal of benz[a]anthracene from cigarette smoke, *Oxford Open Mater. Sci.* 3 (2023), itad012, <https://doi.org/10.1093/oxfmat/itad012>.
- [23] Q. Wang, H. Moriyama, Carbon nanotube-based thin films: synthesis and properties, in: S. Yellampalli (Ed.), *Carbon Nanotubes - Synthesis, Characterization, Applications*, IntechOpen, 2011.
- [24] R.M. Cornell, U. Schwertmann, *The Iron Oxides: Structure, Properties, Reactions, Occurrences and Uses*, Wiley-VCH, Weinheim, 2020.
- [25] R. Bhateria, R. Singh, A review on nanotechnological application of magnetic iron oxides for heavy metal removal, *J. Water Process Eng.* 31 (2019), 100845, <https://doi.org/10.1016/j.jwpe.2019.100845>.
- [26] E.A. Campos, D.V.B.S. Pinto, J.I.S. de Oliveira, E.C. Mattos, R.C.L. Dutra, Synthesis, characterization and applications of iron oxide nanoparticles - a short review, *J. Aerospace Technol. Manage.* 7 (2015) 267–276, <https://doi.org/10.5028/jatm.v7i3.471>.
- [27] S.M. Dadfar, K. Roemhild, N.I. Drude, S. von Stillfried, R. Knüchel, F. Kiessling, T. Lammers, Iron oxide nanoparticles: Diagnostic, therapeutic and theranostic applications, *Adv. Drug Deliv. Rev.* 138 (2019) 302–325, <https://doi.org/10.1016/j.addr.2019.01.005>.
- [28] T. Zhang, J. Ma, Catalytic ozonation of trace nitrobenzene in water with synthetic goethite, *J. Mol. Catal. A Chem.* 279 (2008) 82–89, <https://doi.org/10.1016/j.molcata.2007.09.030>.
- [29] Y. Zhang, J. Yang, J. Du, B. Xing, Goethite catalyzed Cr(VI) reduction by tartaric acid via surface adsorption, *Ecotoxicol. Environ. Saf.* 171 (2019) 594–599, <https://doi.org/10.1016/j.ecoenv.2019.01.024>.
- [30] Q. Liu, Q. Liu, L. Xie, Y. Ji, T. Li, B. Zhang, N. Li, B. Tang, Y. Liu, S. Gao, Y. Luo, L. Yu, Q. Kong, X. Sun, High-Performance electrochemical nitrate reduction to ammonia under ambient conditions using a FeOOH nanorod catalyst, *Appl. Mater. Interfaces* 14 (2022) 17312–17318, <https://doi.org/10.1021/acsami.2c00436>.
- [31] D. Ozturk, M. Gülcen, Synthesis, characterization, and in-situ H₂O₂ generation activity of activated Carbon/Goethite/Fe₃O₄/ZnO for heterogeneous electro-Fenton degradation of organics from woolen textile wastewater, *J. Ind. Eng. Chem.* 122 (2023) 251–263, <https://doi.org/10.1016/j.jiec.2023.02.026>.
- [32] F. Salimi, H. Rahimi, C. Karami, Removal of methylene blue from water solution by modified nanogoethite by Cu, *Desalin. Water Treat.* 137 (2019) 334–344, <https://doi.org/10.5004/dwt.2019.22922>.
- [33] C.R. Nangah, T.G. Merlain, N.J. Nsami, C.P. Tubwoh, J. Foba-Tendo, K. J. Mbadcam, Synthesized goethite and natural iron oxide as effective absorbents for simultaneous removal of Co(II) and Ni(II) ions from water, *J. Encapsulation Adsorption Sci.* 9 (2019) 127–147, <https://doi.org/10.4236/jeas.2019.93007>.
- [34] M.K. Irshad, A. Noman, Y. Wang, Y. Yin, C. Chen, J. Shang, Goethite modified biochar simultaneously mitigates the arsenic and cadmium accumulation in paddy rice (*Oryza sativa*) L, *Environ. Res.* 206 (2022), 112238, <https://doi.org/10.1016/j.envres.2021.112238>.
- [35] I. Janeiro-Tato, D. Baragaño, M.A. Lopez-Anton, E. Rodríguez, A.I. Peláez, R. García, J.R. Gallego, Goethite-based carbon foam nanocomposites for concurrently immobilizing arsenic and metals in polluted soils, *Chemosphere* 301 (2022), 134645, <https://doi.org/10.1016/j.chemosphere.2022.134645>.
- [36] D. Lohse, X. Zhang, Physicochemical hydrodynamics of droplets out of equilibrium, *Nat. Rev. Phys.* 2 (2020) 426–443, <https://doi.org/10.1038/s42254-020-0199-z>.
- [37] K.S. Kolegov, L.Y. Barash, Applying droplets and films in evaporative lithography, *Adv. Colloid Interface Sci.* 285 (2020), 102271, <https://doi.org/10.1016/j.cis.2020.102271>.
- [38] X. Yang, Z. Jiang, P. Lyu, Z. Ding, X. Man, Deposition pattern of drying droplets, *Commun. Theor. Phys.* 73 (2021), 047601, <https://doi.org/10.1088/1572-9494/abda21>.
- [39] Z. Wang, D. Orejon, Y. Takata, K. Sefiane, Wetting and evaporation of multicomponent droplets, *Phys. Rep.* 960 (2022) 1–37, <https://doi.org/10.1016/j.physrep.2022.02.005>.
- [40] S.K. Wilson, H.M. D'Ambrosio, Evaporation of Sessile Droplets, *Annu. Rev. Fluid Mech.* 55 (2023) 481–509, <https://doi.org/10.1146/annurev-fluid-031822-013213>.
- [41] I.Y. Tóth, L. Janovák, E.S. Bogya, Á. Deák, I. Dékány, A. Rawal, Á. Kukovecz, Characterization of the solvent specific evaporation from a fluoropolymer surface roughened by layered double oxide (LDO) particles, *J. Mol. Liq.* 305 (2020), 112826, <https://doi.org/10.1016/j.jmolliq.2020.112826>.
- [42] A. Akanno, L. Perrin, E. Guzmán, S. Llamas, V.M. Starov, F. Ortega, R.G. Rubio, M. G. Velarde, Evaporation of sessile droplets of polyelectrolyte/surfactant mixtures on silicon wafers, *Colloids Interfaces* 5 (2021) 12, <https://doi.org/10.3390/colloids5010012>.
- [43] L. Perrin, A. Pajor-Swierzy, S. Magdasi, A. Kamysny, F. Ortega, R.G. Rubio, Evaporation of nanosuspensions on substrates with different hydrophobicity, *Appl. Mater. Interfaces* 10 (2018) 3082–3093, <https://doi.org/10.1021/acsami.7b15743>.
- [44] G. Schusztar, E.S. Bogya, D. Horváth, Á. Tóth, H. Haspel, Á. Kukovecz, Liquid droplet evaporation from buckypaper: on the fundamental properties of the evaporation profile, *Microporous Mesoporous Mater.* 209 (2015) 105–112, <https://doi.org/10.1016/j.micromeso.2015.02.025>.
- [45] V.M. Starov, S.R. Kostvintsev, V.D. Sobolev, M.G. Velarde, S.A. Zhdanov, Spreading of liquid drops over dry porous layers: complete wetting case, *J. Colloid Interface Sci.* 252 (2002) 397–408, <https://doi.org/10.1006/jcis.2002.8450>.
- [46] V.M. Starov, S.A. Zhdanov, M.G. Velarde, Spreading of liquid drops over thick porous layers: complete wetting case, *Langmuir* 18 (2002) 9744–9750, <https://doi.org/10.1021/la025759y>.
- [47] V.M. Starov, S.A. Zhdanov, S.R. Kostvintsev, V.D. Sobolev, M.G. Velarde, Spreading of liquid drops over porous substrates, *Adv. Colloid Interface Sci.* 104 (2003) 123–158, [https://doi.org/10.1016/S0001-8686\(2003\)00039-3](https://doi.org/10.1016/S0001-8686(2003)00039-3).
- [48] N. Shokri, M. Sahimi, D. Or, Morphology, propagation dynamics and scaling characteristics of drying fronts in porous media, *Geophys. Res. Lett.* 39 (2012) L09401, <https://doi.org/10.1029/2012GL051506>.
- [49] R. Wu, G.M. Cui, R. Chen, Pore network study of slow evaporation in hydrophobic porous media, *Int. J. Heat Mass Transfer* 68 (2014) 310–323, <https://doi.org/10.1016/j.jheatmasstransfer.2013.09.042>.
- [50] S. David, K. Sefiane, L. Tadrist, Experimental investigation of the effect of thermal properties of the substrate in the wetting and evaporation of sessile drops, *Colloids Surf. A Physicochem. Eng. Asp.* 298 (2007) 108–114, <https://doi.org/10.1016/j.colsurfa.2006.12.018>.
- [51] E. Nefzaoui, O. Skurtys, Impact of a liquid drop on a granular medium: inertia, viscosity and surface tension effects on the drop deformation, *Exp. Therm Fluid Sci.* 41 (2012) 43–50, <https://doi.org/10.1016/j.expthermflusci.2012.03.007>.
- [52] E.S. Bogya, B. Szilagy, Á. Kukovecz, Surface pinning explains the low heat transfer coefficient between water and a carbon nanotube film, *Carbon* 100 (2016) 27–35, <https://doi.org/10.1016/j.carbon.2015.12.077>.
- [53] L. Wang, J. Qin, Z. Bai, Y. Hao, W. Li, J. Wang, X. Li, Core-branched FeOOH-CNTs composites for high-performance supercapacitors, *Mater. Lett.* 322 (2022), 132442, <https://doi.org/10.1016/j.matlet.2022.132442>.
- [54] P.Q. Yang, T.E. Ko, C.M. Tseng, W.H. Wang, C.C. Huang, J.E. Tsai, Y.C. Fu, Y.Y. Li, FeOOH-carbon nanotube-FeCo/nitrogen-doped porous carbon as an excellent bifunctional catalyst for achieving high power performance in rechargeable zinc-air batteries, *J. Ind. Eng. Chem.* 121 (2023) 338–347, <https://doi.org/10.1016/j.jiec.2023.01.037>.
- [55] D. Fu, Z. He, S. Su, B. Xu, Y. Liu, Y. Zhao, Fabrication of α -FeOOH decorated graphene oxide-carbon nanotubes aerogel and its application in adsorption of arsenic species, *J. Colloid Interface Sci.* 505 (2017) 105–114, <https://doi.org/10.1016/j.jcis.2017.05.091>.
- [56] X. Hu, Y. Liu, F. Liu, H. Jiang, F. Li, C. Shen, X. Fang, J. Yang, Simultaneous decontamination of arsenite and antimonite using an electrochemical CNT filter functionalized with nanoscale goethite, *Chemosphere* 274 (2021), 129790, <https://doi.org/10.1016/j.chemosphere.2021.129790>.
- [57] A. Kukovecz, Z. Konya, N. Nagaraju, I. Willems, A. Tamasi, A. Fonseca, J.B. Nagy, I. Kiricsi, Catalytic synthesis of carbon nanotubes over Co, Fe and Ni containing conventional and sol-gel silica-aluminas, *Phys. Chem. Chem. Phys.* 2 (2000) 3071–3076, <https://doi.org/10.1039/B002331K>.
- [58] C.E. Kozonoe, R. Giudici, M. Schmal, Ruthenium catalyst supported on multi-walled carbon nanotubes for CO oxidation, *Modern Res. Catal.* 10 (2021) 73–91, <https://doi.org/10.4236/mrc.2021.103005>.
- [59] F.H. Abdulrazzak, A.F. Alkiam, F.H. Hussein, Behavior of X-Ray Analysis of Carbon Nanotubes, in: H.E.D. Saleh, S.M.M. El-Sheikh (Eds.), *Chapter 7 Perspective of Carbon Nanotubes*, BoD-Books on Demand, 2019.
- [60] X. Zhao, Y. Ando, Raman spectra and X-ray diffraction patterns of carbon nanotubes prepared by hydrogen arc discharge, *Jpn. J. Appl. Phys.* 37 (1998) 4846–4849, <https://doi.org/10.1143/JJAP.37.4846>.
- [61] Y. Shao, G. Hu, Z. Liu, X. Xu, M. Zhang, C. Ding, Y. Li, Determination of band structure of naturally occurring goethite with Al substitution: a case study of zhushan iron zone, *Materials* 15 (2022) 1465, <https://doi.org/10.3390/ma15041465>.
- [62] M. Flygare, K. Svensson, Quantifying crystallinity in carbon nanotubes and its influence on mechanical behaviour, *Mater. Today Commun.* 18 (2019) 39–45, <https://doi.org/10.1016/j.mtcomm.2018.11.003>.
- [63] M. Kosmulski, Isoelectric points and points of zero charge of metal (hydr)oxides: 50 years after Parks' review, *Adv. Colloid Interface Sci.* 238 (2016) 1–61, <https://doi.org/10.1016/j.cis.2016.10.005>.
- [64] G. Sposito, Characterization of particle surface charge, in: J. Buffle, H.P. van Leeuwen (Eds.), *Environmental Particles*, Lewis, Boca Raton, 1992.
- [65] J. Lyklema, *Fundamentals of Interface and Colloid Science*, Academic Press, London, 1995.
- [66] L. Vanyorek, R. Meszaros, S.R. Barany, Surface and electrochemical characterization of surface-oxidized multi-walled N-doped carbon nanotubes, *Colloids Surf. A:*

- Physicochem. Eng. Aspects 448 (2014) 140–146, <https://doi.org/10.1016/j.colsurfa.2014.01.078>.
- [67] T.L.A. Montanheiro, F.H. Cristóvan, J.P.B. Machado, D.B. Tada, N. Durán, A. P. Lemes, Effect of MWCNT functionalization on thermal and electrical properties of PHBV/MWCNT nanocomposites, *J. Mater. Res.* 30 (2015) 55–65, <https://doi.org/10.1557/jmr.2014.303>.
- [68] C.T. Johnston E. Tombácz Surface chemistry of soil minerals, in: J.B. Dixon, D. G. Schulze (Eds.) *Soil Mineralogy with Environmental Applications 2002 SSSA*, Madison, Wisconsin.
- [69] S. Dultz, H. Steinke, R. Mikutta, S.K. Woche, G. Guggenberger, Impact of organic matter types on surface charge and aggregation of goethite, *Colloids Surf. A Physicochem. Eng. Asp* 554 (2018) 156–168, <https://doi.org/10.1016/j.colsurfa.2018.06.040>.
- [70] E. Illés, E. Tombácz, The role of variable surface charge and surface complexation in the adsorption of humic acid on magnetite, *Colloids Surf. A Physicochem. Eng. Asp* 230 (2006) 99–109, <https://doi.org/10.1016/j.colsurfa.2003.09.017>.
- [71] R.O. James, G.A. Parks, Characterization of aqueous colloids by their electrical double-layer and intrinsic surface chemical properties, in: E. Matijevic (Ed.), *Surface and Colloid Science*, Plenum Press, New York, 1982.
- [72] S. Panić, D. Rakić, V. Guzsvány, E. Kiss, G. Boskovic, Z. Kónya, Á. Kukovecz, Optimization of thiamethoxam adsorption parameters using multi-walled carbon nanotubes by means of fractional factorial design, *Chemosphere* 141 (2015) 87–93, <https://doi.org/10.1016/j.chemosphere.2015.06.042>.
- [73] L. Stobinski, B. Lesiak, L. Kövér, J. Tóth, S. Biniak, G. Trykowski, J. Judek, Multiwall carbon nanotubes purification and oxidation by nitric acid studied by the FTIR and electron spectroscopy methods, *J. Alloy. Compd.* 501 (2010) 77–84, <https://doi.org/10.1016/j.jallcom.2010.04.032>.
- [74] B.A. Kakade, V.K. Pillai, Tuning the wetting properties of multiwalled carbon nanotubes by surface functionalization, *J. Phys. Chem. C* 112 (2008) 3183–3186, <https://doi.org/10.1021/jp711657f>.
- [75] J. Debgupta, B.A. Kakade, V.K. Pillai, Competitive wetting of acetonitrile and dichloromethane in comparison to that of water on functionalized carbon nanotube surfaces, *Phys. Chem. Chem. Phys.* 13 (2011) 14668–14674, <https://doi.org/10.1039/C1CP21121H>.
- [76] M. Veneranda, J. Aramendia, L. Bellot-Gurlet, P. Colomban, K. Castro, J. M. Madariaga, FTIR spectroscopic semi-quantification of iron phases: a new method to evaluate the protection ability index (PAI) of archaeological artefacts corrosion systems, *Corros. Sci.* 133 (2018) 68–77, <https://doi.org/10.1016/j.corsci.2018.01.016>.
- [77] R. Liu, S. Kong, Y. Shao, D. Cai, B. Bai, X. Wei, R.A. Root, X. Gao, C. Li, J. Chorover, Mechanisms and health implications of toxicity increment from arsenate-containing iron minerals through in vitro gastrointestinal digestion, *Geoderma* 432 (2023), 116377, <https://doi.org/10.1016/j.geoderma.2023.116377>.
- [78] J. Zhang, D. Jiang, H.-X. Peng, A pressurized filtration technique for fabricating carbon nanotube buckypaper: Structure, mechanical and conductive properties, *Microporous Mesoporous Mater.* 184 (2014) 127–133, <https://doi.org/10.1016/j.micromeso.2013.10.012>.
- [79] D.E. Hinkle, W. Wiersma, S.G. Jurs, *Applied Statistics for the Behavioral Sciences, fifth ed.*, Houghton Mifflin, Boston, 2003.
- [80] G. Rugg, *Using Statistics: A Gentle Introduction*, first ed., McGraw-Hill, Maidenhead, 2007.